Numerical Simulation of the Effect of Spatial Disturbances on Vortex Asymmetry

David Degani* and Lewis B. Schiff†
NASA Ames Research Center, Moffett Field, California 94035

The steady asymmetric vortex pattern observed on slender bodies of revolution at large angle of attack was investigated using fine-grid, thin-layer Navier-Stokes computations. The computed results demonstrate, for the first time, the marked asymmetry that has been observed in experiments. To obtain asymmetry, it was found essential to introduce a space-fixed, time-invariant perturbation into the computation. If the perturbation was removed, the asymmetric flow returned toward symmetry. The perturbations were found to be more effective when located close to the nose. Taken together with the experimental observations, the computational results suggest that vortex asymmetry is forced by amplification of small disturbances, such as those due to surface roughness, occurring within the body viscous boundary layer.

Introduction

THE onset of vortex asymmetry on the forebody of a flight vehicle maneuvering at large angles of attack can generate unwanted yawing moments, which can lead to departure from controlled flight. This phenomenon is typified by the vortex asymmetry observed in the flow about slender bodies of revolution at large incidence. As a result, over the past three decades, a large number of researchers have investigated high angle-of-attack flow over slender axisymmetric bodies. The recent survey articles by Hunt[1] and Ericsson and Reding[2] provide extensive bibliographies of these investigations.

The flow observed about a slender body of revolution placed at incidence to an oncoming stream exhibits a wide variety of phenomena. As the angle of attack is increased from zero, a steady, symmetric pair of vortices is observed in the leeward-side flow. With further increase in incidence, the symmetric vortex pair is observed to become asymmetric, but remains steady in time. At still higher incidence, the steady asymmetric pair evolves to a steady pattern of multiple vortices that leave from alternate sides of the body with increasing distance downstream (cf. Ref. 3 for extensive examples of steady alternate shedding of multiple vortices illustrated through flow-visualization photos). With further increase in incidence, the asymmetric flow becomes unsteady, and as the angle of attack tends toward 90 deg, the flow pattern approaches that of a circular cylinder in crossflow.

Flow over a slender axisymmetric body at $\alpha = 90$ deg is (except for the region near the nose) the classical flow observed about a two-dimensional cylinder in crossflow. It is well known that at low Reynolds numbers, flow about the cylinder is steady and symmetric. However, when the Reynolds number is increased beyond a critical value ($Re_D \approx 50$) the flow becomes unsteady. Vortices are shed periodically from alternate sides of the cylinder and are convected downstream to form the classic Karman vortex street. This transition from a steady to an unsteady, periodic flow is known as a Hopf bifurcation (cf. Ref. 4 for a discussion of bifurcations in aerodynamics).

Received July 18, 1989; revision received March 28, 1990. Copyright © 1990 by the American Institute of Aeronautics and Astronautics, Inc. No copyright is asserted in the United States under Title 17, U.S. Code. The U.S. Government has a royalty-free license to exercise all rights under the copyright claimed herein for Governmental purposes. All other rights are reserved by the copyright owner.

*National Research Council Senior Research Associate; also Associate Professor, Technion-Israel Institute of Technology, Faculty of Mechanical Engineering. Associate Fellow AIAA.

†Special Assistant for High Alpha Technology, Fluid Dynamics Division. Associate Fellow AIAA.

Time-accurate computations of two-dimensional flow about the circular cylinder[5-7] (using algorithms that are unbiased in the circumferential direction) have found that, unless a perturbation was introduced into the flow to trigger the asymmetry, the solutions remained symmetric and steady. The pertubations were typically introduced for a short period of time, then removed, and the flows advanced in time until the periodic solution developed.

In Ref. 8, we utilized the time-accurate, thin-layer Navier-Stokes code reported by Steger et al.[9] to study the three-dimensional subsonic flow surrounding a slender body of revolution at large incidence. Initial computed results for the flow surrounding an ogive-cylinder body at $M_\infty = 0.2$, $\alpha = 40$ deg, and Reynolds number (based on freestream conditions and cylinder diameter) $Re_D = 2 \times 10^5$ indicated that the computed flow remained symmetric at angles of attack where experimental measurements showed the presence of large asymmetry. Guided by the results for the two-dimensional cylinder flow, a transient symmetry-breaking perturbation was applied to induce asymmetry. When the perturbation (a small surface jet blowing normal to the surface and perpendicular to the angle of attack plane) was introduced, the solution started to evolve to an asymmetric state. However, in contrast to the computations for two-dimensional Karman shedding, when the perturbation was removed, the asymmetric solution returned to symmetry. When a space-fixed, time-invariant perturbation was used (i.e., the jet, once introduced, was kept constant for all time), the computed flow reached and maintained an asymmetric state.

Even with the use of methods based on the Navier-Stokes equations, computation of the asymmetric vortex flow on bodies at large incidence has not been straightforward. Graham and Hankey[10] used a Navier-Stokes code based on MacCormack's noncentered algorithm to compute three-dimensional viscous flow around a slender cone-cylinder body at $M_\infty = 1.6$, $\alpha = 30$ deg, and Reynolds number (based on body length) $Re_L = 4 \times 10^5$. Their results showed only a tiny asymmetry in the computed flowfield, which they attributed to built-in asymmetries in the numerical algorithm. On the other hand, experimental measurements for this case[3] show a marked asymmetry. Zilliac,[11] using an implicit incompressible Navier-Stokes method to compute flow over a short ogive-cylinder body at angles of attack up to 45 deg at $Re_L = 10^3$, found that the computed flowfields were perfectly symmetric.

Several experimental studies of bodies of revolution at large incidence (cf. Refs. 12–16) have shown that multiple values of side force can be obtained at a fixed angle of attack and Reynolds number, depending on the roll orientation of the body. In particular, Lamont[12,13] and Dexter and Hunt[14] found

evidence of symmetric flows at angles of attack where most of their measurements showed large asymmetry. Hall,[15] analyzing Lamont's data, showed the existence of a range of side force values at a fixed incidence. These computational and experimental observations lead us to believe that three-dimensional vortex asymmetry on slender bodies at large incidence is forced by space-fixed, time-fixed disturbances, such as those due to surface roughness.

In the current work, we have applied thin-layer Navier-Stokes computations to further investigate the phenomena governing onset of vortex asymmetry. Time-accurate solutions were obtained for flow over the ogive-cylinder body considered in Ref. 8. To examine whether multiple asymmetric states can be obtained computationally, a small jet acting normal to the angle-of-attack plane was used as a space-fixed, time-invariant perturbation. The effect on the resulting flow of differing jet locations was investigated. In addition, the effect on the computed flows of variation in freestream Reynolds number was examined.

Theoretical Background

Governing Equations

The conservation equations of mass, momentum, and energy can be represented in a flux-vector form that is convenient for numerical simulation as[17]

$$\partial_\tau \hat{Q} + \partial_\xi(\hat{F} + \hat{F}_v) + \partial_\eta(\hat{G} + \hat{G}_v) + \partial_\zeta(\hat{H} + \hat{H}_v) = 0 \tag{1}$$

where τ is the time and the independent spatial variables ξ, η, and ζ are chosen to map a curvilinear body-conforming grid into a uniform computational space. In Eq. (1), $\hat{Q}$ is the vector of dependent flow variables; $\hat{F} = \hat{F}(\hat{Q})$, $\hat{G} = \hat{G}(\hat{Q})$, and $\hat{H} = \hat{H}(\hat{Q})$ are the inviscid flux vectors, while the terms $\hat{F}_v$, $\hat{G}_v$, and $\hat{H}_v$ are fluxes containing the viscous derivatives. A nondimensional form of the equations is used throughout this work. The conservative form of the equations is maintained chiefly to capture shock waves in transonic and supersonic flows as accurately as possible.

For body-conforming coordinates and high Reynolds number flow, if ζ is the coordinate leading away from the surface, the thin-layer approximation can be applied, which yields[18,19]

$$\partial_\tau \hat{Q} + \partial_\xi \hat{F} + \partial_\eta \hat{G} + \partial_\zeta \hat{H} = Re^{-1}\partial_\zeta \hat{S} \tag{2}$$

where only viscous terms in ζ are retained. These have been collected into the vector $\hat{S}$, and the nondimensional Reynolds number Re is factored from the viscous flux term. The validity of applying the thin-layer approximate in computations of high-incidence separated flows was demonstrated in Refs. 20 and 21. The coefficients of viscosity and thermal conductivity that appear in Eq. (2) are specified from auxiliary relations. For laminar flow, the coefficient of viscosity is obtained using Sutherland's law. The coefficient of thermal conductivity is obtained once the viscosity coefficient is known by assuming a constant Prandtl number.

In differencing these equations, it is often advantageous to difference about a known base solution denoted by subscript o as follows

$$\begin{aligned}&\delta_\tau(\hat{Q} - \hat{Q}_o) + \delta_\xi(\hat{F} - \hat{F}_o) + \delta_\eta(\hat{G} - \hat{G}_o)\\ &\quad + \delta_\zeta(\hat{H} - \hat{H}_o) - Re^{-1}\delta_\zeta(\hat{S} - \hat{S}_o) =\\ &\quad - \partial_\tau \hat{Q}_o - \partial_\xi \hat{F}_o - \partial_\eta \hat{G}_o - \partial_\zeta \hat{H}_o + Re^{-1}\partial_\zeta \hat{S}_o\end{aligned} \tag{3}$$

where δ indicates a general difference operator and ∂ is the differential operator. If the base state is properly chosen, the differenced quantities can have smaller and smoother variation and, therefore, less differencing error. In particular, errors introduced into the solution by the finite difference approximations of the spatial metrics can be reduced. In the current application, the freestream is used as the base solution and the right side of Eq. (3) is zero.

Numerical Algorithm

The implicit scheme employed in this study is the algorithm reported by Steger et al.[9] The algorithm uses flux-vector splitting[20] and upwind spatial differencing for the convection terms in one coordinate direction (nominally streamwise). As discussed in Ref. 9, schemes using upwind differencing can have several advantages over methods that utilize central spatial differences in each direction. In particular, such schemes can have natural numerical dissipation and better stability properties. By using upwind differencing for the convective terms in the streamwise direction while retaining central differencing in the other directions, a two-factor implicit approximately factored algorithm is obtained, which is unconditionally stable[21] for a representative model wave equation. The scheme may be written for the thin-layer Navier-Stokes equations in the form

$$\begin{aligned}&[I + h\delta_\xi^b(\hat{A}^+)^n + h\delta_\zeta \hat{C}^n - hRe^{-1}\bar{\delta}_\zeta J^{-1}\hat{M}^n J - D_i|_\zeta]\\ &\quad \times [I + h\delta_\xi^f(\hat{A}^-)^n + h\delta_\eta \hat{B}^n - D_i|_\eta]\Delta\hat{Q}^n =\\ &\quad - \Delta t\{\delta_\xi^b[(\hat{F}^+)^n - \hat{F}_\infty^+] + \delta_\xi^f[(\hat{F}^-)^n - F_\infty^-]\\ &\quad + \delta_\eta(\hat{G}^n - \hat{G}_\infty) + \delta_\zeta(\hat{H}^n - \hat{H}_\infty)\\ &\quad - Re^{-1}\bar{\delta}_\zeta(\hat{S}^n - \hat{S}_\infty)\} - D_e(\hat{Q}^n - \hat{Q}_\infty)\end{aligned} \tag{4}$$

where $h = \Delta t$ or $\Delta t/2$ for first- or second-order time accuracy, and the freestream base solution is used. Second-order time accuracy is used throughout this work since an unsteady solution is required. In Eq. (4), δ is typically a three-point, second-order-accurate, central difference operator, $\bar{\delta}$ is a midpoint operator used with the viscous terms, and the operators δ_ξ^b and δ_ξ^f are backward and forward three-point difference operators. The flux $\hat{F}$ has been split into $\hat{F}^+$ and $\hat{F}^-$, according to its eigenvalues,[20] and the matrices $\hat{A}^\pm$, $\hat{B}$, $\hat{C}$, and $\hat{M}$ result from local linearization of the fluxes about the previous time level. J denotes the Jacobian of the coordinate transformation. Dissipation operators D_e and D_i are used in the central space differencing directions. Full details of the development of the algorithm may be found in Refs. 9 and 21.

Numerical Smoothing

The finite difference scheme uses flux splitting in the ξ direction and central differencing in the η and ζ directions. As a consequence, numerical dissipation terms denoted by D_i and D_e in Eq. (4) are employed in the η and ζ directions and are given as combinations of second and fourth differences. The smoothing terms are of the form

$$D_e|_\eta = (\Delta t)J^{-1}\{\epsilon_2\bar{\delta}|\hat{B}|\beta\bar{\delta} + \epsilon_4\bar{\delta}\frac{|\hat{B}|}{1+\beta}\bar{\delta}^3\}|_\eta J \tag{5a}$$

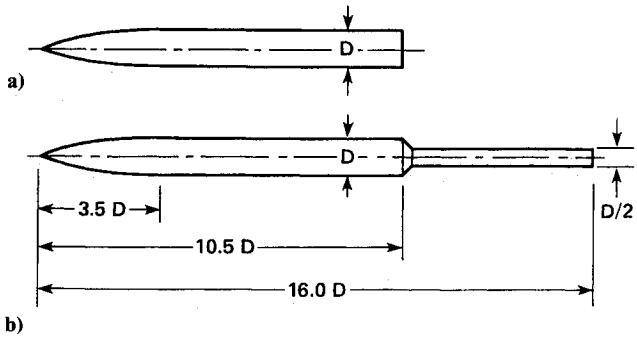

Fig. 1 Ogive-cylinder configurations.

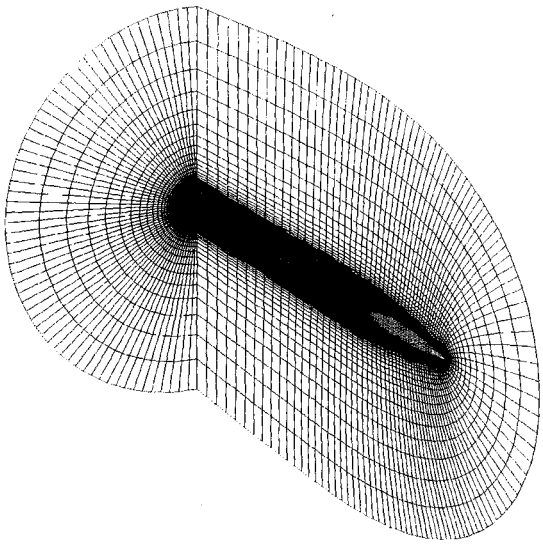

Fig. 2 Tangent ogive-cylinder grid.

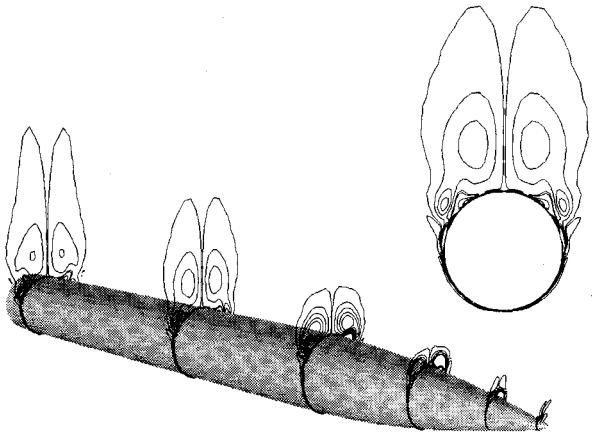

Fig. 3 Helicity density contours: $M_\infty = 0.2$, $\alpha = 40$ deg, $Re_D = 2 \times 10^5$ (no jet).

$$D_i|_\eta = (\Delta t)J^{-1}\{\epsilon_2\bar{\delta}|\hat{B}|\beta\bar{\delta} + 2.5\epsilon_4\bar{\delta}\frac{|\hat{B}|}{1+\beta}\bar{\delta}^3\}|_\eta J \tag{5b}$$

where

$$\beta = \frac{|\bar{\delta}^2 p|}{|(1+\bar{\delta}^2)p|}$$

and where $|\hat{B}|$ is the spectral radius of the matrix $\hat{B}$ or an approximation. Here, p is the nondimensional fluid pressure and ϵ_2 $\mathcal{O}(1 + M_\infty^\gamma)$, whereas ϵ_4 is $\mathcal{O}$ (0.01). In this form, the second-order smoothing terms act to control numerical oscillations across shock waves, and the fourth-order smoothing is effective elsewhere. In order to improve the accuracy of the solutions, the fourth-order numerical smoothing terms are further scaled by q/q_∞. This has the effect of reducing the numerical smoothing in the viscous layer adjoining the body surface where large numerical smoothing terms can adversely affect the accuracy of the solution by modifying the physical viscous terms.

Body Configurations and Computational Grids

Computations were performed for subsonic flow over the two ogive-cylinder bodies shown in Fig. 1. Configuration A consisted of a 3.5-diam tangent ogive forebody with a 7.0-diam cylindrical afterbody extending aft of the nose-body junction to $x/D = 10.5$. Configuration B was identical to body A, but had a 0.5-body-diam sting that extended an additional 5.5 diam downstream, to $x/D = 16.0$. These bodies were selected for study because an ogive-cylinder body having a 3.5-diam tangent ogive nose and a 4.0-diam cylindrical afterbody had been extensively tested by Lamont[13] in the NASA Ames 12-ft Pressure Wind Tunnel. In that experiment, detailed surface pressure distributions were obtained at Reynolds numbers ranging from $Re_D = 2 \times 10^5$ to 4×10^6, and at angles of attack ranging from $\alpha = 20$ to 90 deg.

The grid used for numerical simulation of the flow about configuration A is shown in Fig. 2. The grid consists of 120 equispaced circumferential planes ($\Delta\phi = 3$ deg) extending completely around the body. In each circumferential plane, the grid contained 50 radial points between the body surface and the computational outer boundary and 59 axial points between the nose and the rear of the body. For configuration B, an additional 10 axial points were used to model the sting.

Boundary Conditions and Initial Conditions

An adiabatic no-slip boundary condition was applied at the body surface, while undisturbed freestream conditions were maintained at the computational outer boundary. An implicit periodic continuation condition was imposed at the circumferential edges of the grid, while at the downstream boundary, a simple zero-axial-gradient extrapolation condition was applied. This simple extrapolation boundary condition is not strictly valid in subsonic flow since the body wake can affect the flow on the body. However, by letting both computed body lengths extend beyond the physical length of the experimental model,[13] and neglecting the portion of the flow near the downstream boundary, we can minimize the effect of the boundary. On the upstream axis of symmetry, an extrapolation boundary condition was used to obtain the flow conditions on the axis from the cone of points one axial plane downstream.

In these computations, a time-accurate solution is required. Thus, the second-order time-accurate algoithm is used with a globally constant time step. The flowfield was initially set to freestream conditions throughout the grid, or to a previously obtained solution, and the flowfield was advanced in time until a solution was obtained.

A weak jet was imposed on the body surface as a symmetry-breaking perturbation. Two jet locations were used: an upstream jet located at $x/D \approx 0.12$ and a downstream jet located at $x/D \approx 1.20$. Both jets were located 90 deg circumferentially from the windward meridian, that is, acting perpendicular to the angle of attack plane on the right side of the body (viewed from behind and looking upstream). A small normal momentum was imposed and maintained constant as the solutions evolved.

The code requires approximately 8×10^{-5} s/iteration/grid point on the NAS CRAY-2 computer. This translates to approximately 27 s/iteration for the smaller grid and approximately 32 s/iteration for the larger grid. Further, the need to resolve the thin viscous layers for high Reynolds number flow requires that the grids have a fine radial spacing at the body

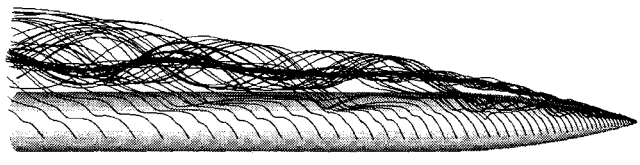

Fig. 4 Off-surface streamlines: $M_\infty = 0.2$, $\alpha = 40$ deg, $Re_D = 2 \times 10^5$ (no jet).

Fig. 5 Surface flow pattern: $M_\infty = 0.2$, $\alpha = 40$ deg, $Re_D = 2 \times 10^5$ (no jet).

surface. As a result, the allowable computational nondimensional time steps were found to range from 0.005 to 0.010.

Results

The four computations presented here were all obtained for $M_\infty = 0.2$ and $\alpha = 40$ deg. Except for case 4, the computations were all carried out for a Reynolds number based on body diameter, Re_D, of 2×10^5. Case 1 is the symmetric flow that was obtained in grid A when the jet strength was set to zero. Case 2 is the asymmetric flow obtained in grid B when the symmetry-breaking jet was located approximately 1.20 body diam downstream from the nose. Case 3 is similar and was obtained using grid A with the jet located further upstream, approximately 0.12 body diam from the nose. For case 4, grid B was used with the jet located 0.12 diam from the nose and with $Re_D = 2.6 \times 10^4$. This Reynolds number was chosen to match the conditions used by Degani and Zilliac[22] in a complementary experimental investigation of vortex asymmetry and vortex unsteadiness.

Case 1 – Symmetric Flow

Results for case 1 are presented in Figs. 3–6. In this computation, the jet strength was zero and the computed flow remained symmetric about the angle-of-attack plane. Although the computed flow was found to be unsteady, the unsteadiness produces only small changes relative to mean flow, and, thus, the main flow features can be seen in the "snapshots" shown later. A companion computational study of vortex unsteadiness is contained in Ref. 23.

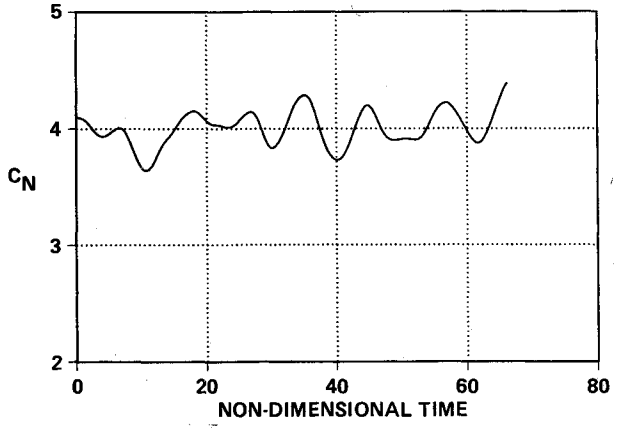

Fig. 6 Normal-force coefficient history: $M_\infty = 0.2$, $\alpha = 40$ deg, $Re_D = 2 \times 10^5$.

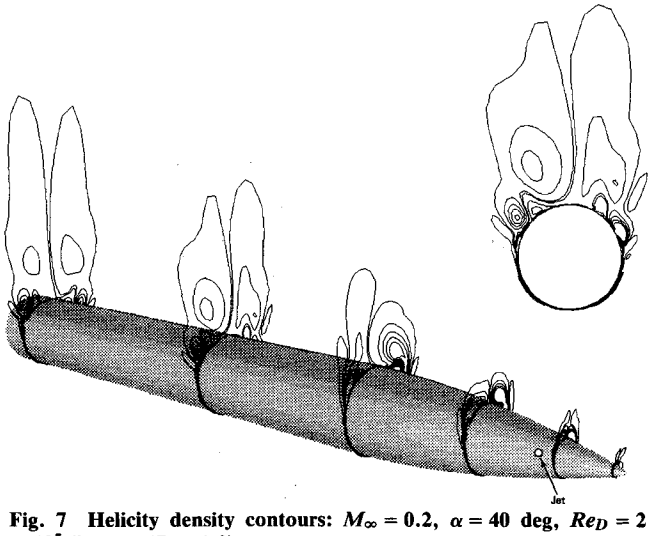

Fig. 7 Helicity density contours: $M_\infty = 0.2$, $\alpha = 40$ deg, $Re_D = 2 \times 10^5$ (jet at $x/D \approx 1.2$).

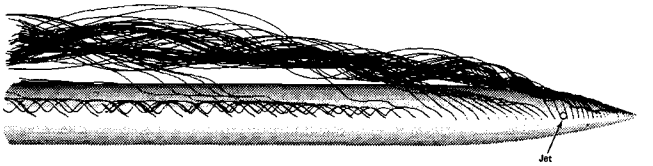

Fig. 8 Off-surface streamlines : $M_\infty = 0.2$, $\alpha = 40$ deg, $Re_D = 2 \times 10^5$ (jet at $x/D \approx 1.2$).

Fig. 9 Surface flow pattern: $M_\infty = 0.2$, $\alpha = 40$ deg, $Re_D = 2 \times 10^5$ (jet at $x/D \approx 1.2$).

Computed helicity density contours in several cross sections on the forward part of the body ($0 \leq x/D \leq 9.9$) are shown in Fig. 3. Details of the cross section located at $x/D = 5.6$ are repeated in the upper right corner of the figure. Helicity density is defined as the scalar product of the local velocity and vorticity vectors. Since it indicates both the strength and sense of rotation of the vortices, helicity density has been found to be an excellent means of visualizing the position and strength of the vortex pattern.[24] By marking positive and negative values of helicity with different colors, it is easy to differentiate between the primary and secondary vortices. Although both positive and negative helicity contours are presented in Fig. 3, the monochromatic figures cannot explicitly indicate the sense of rotation of the vortices. However, the location of the primary crossflow separation on the side of the body and the growth in size and height of the primary and secondary vortices with increasing distance downstream is seen easily.

The location and rotation of the primary leeward-side vortices are also evident in the off-surface streamline pattern presented in Fig. 4. The two vortices that originate at the nose run almost parallel to the body upper surface as they grow with distance downstream. In contrast to the results obtained experimentally,[22] the computed vortices do not appear to lift away from the body surface. It should be noted that the lift off of the vortices seems to be linked with the asymmetry in the experimental flow. Indeed, experiments[25] conducted in the smoke tunnel using a splitter plate to enforce symmetry of the leeward-side flow indicated that only one pair of primary vortices was present and that they tended to remain close to the body surface.

The computed leeward-side surface flow pattern is shown in Fig. 5 and confirms that the computed flow remains symmetric. However, the flow is not steady. As reported previously,[8] the shear layers that emanate from the primary separation lines and roll up to form the primary vortices exhibit a small-scale nonsteadiness. For the current computations, a change in the code reduced the effect of the numerical smoothing terms near the wall. As a result, the nonsteadiness exhibited more frequencies than was observed previously. This can be seen from the segment of the normal-force coefficient time history shown in Fig. 6. In contrast to the almost periodic behavior of the normal force obtained previously, the normal force is oscillating in a more arbitrary manner. The scale of the fluctuations relative to the mean value of the normal-force coefficient can also be seen in Fig. 6.

Case 2 – Asymmetric Flow, Downstream Jet

At 40-deg angle of attack, the experimental flow was asymmetric, whereas the computed flow remained perfectly symmetric. To break the symmetry of the solution, a time-invariant, space-fixed disturbance was added to the flowfield discussed earlier. A small jet having a strength of about 0.1% of the total normal force was introduced at $x/D \approx 1.2$, blowing normal to the body axis and oriented perpendicular to the

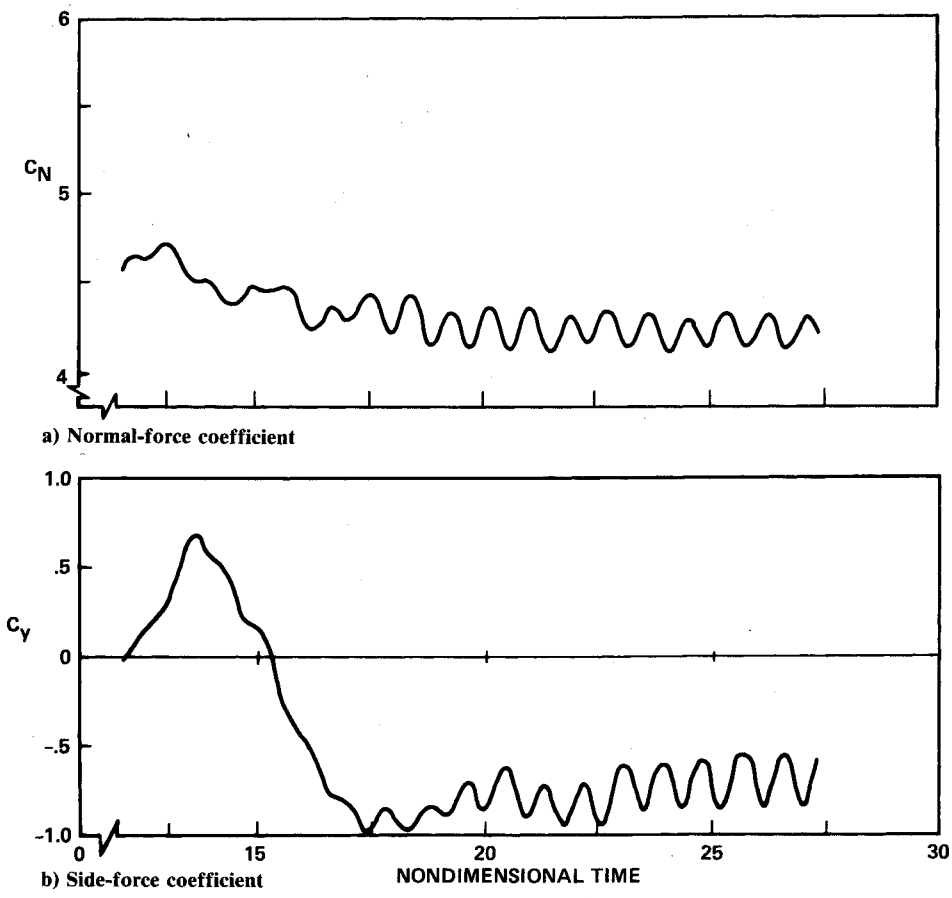

Fig. 10 Force coefficient histories: $M_\infty = 0.2$, $\alpha = 40$ deg, $Re_D = 2 \times 10^5$ (jet at $x/D \approx 1.2$).

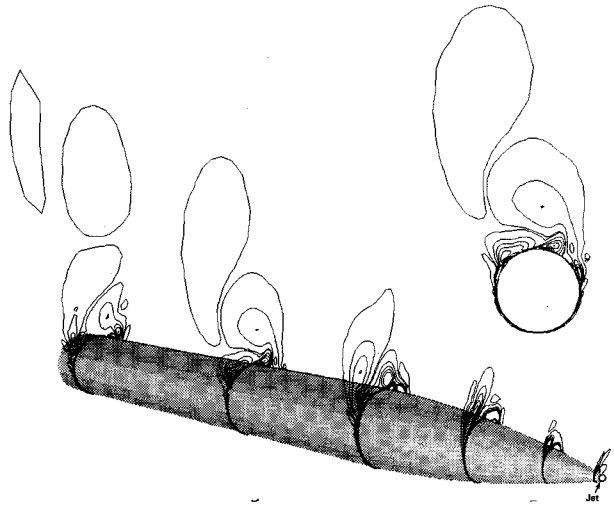

Fig. 11 Helicity density contours: $M_\infty = 0.2$, $\alpha = 40$ deg, $Re_D = 2 \times 10^5$ (jet at $x/D \approx 0.12$).

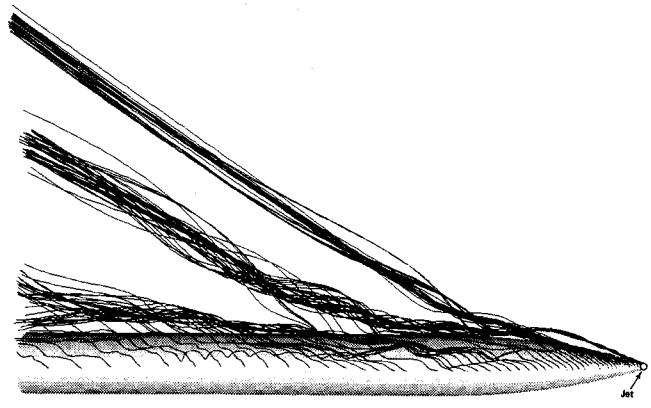

Fig. 12 Off-surface streamlines: $M_\infty = 0.2$, $\alpha = 40$ deg, $Re_D = 2 \times 10^5$ (jet at $x/D \approx 0.12$).

angle-of-attack plane on the right side of the body. Although the resulting flow is no longer symmetric, the asymmetry is relatively small. This can be seen from the computed helicity density contours shown in Fig. 7, the off-surface streamline pattern shown in Fig. 8, and the leeward-side surface flow pattern shown in Fig. 9. In this case, the vortices still lie close to the leeward body surface.

The normal-force coefficient time history for this case is shown in Fig. 10a, while the side-force coefficient history is shown in Fig. 10b. These force histories were previously presented in Ref. 2, but are included here for the sake of completeness. In this computation, an earlier type of numerical smoothing was used, which resulted in a greater smoothing near the wall. As a result, after the initial transient dies away, both force histories show a smooth periodic oscillation. The oscillatory excursions are small compared to the mean values of the coefficients.

As shown in Fig. 10b, the mean value of the side-force coefficient is approximately -0.7. This side force is about 100 times larger than the net force due to jet itself. Two numerical experiments were conducted to investigate the stability of the asymmetric solution. Both experiments started from the solution obtained at time = 27.5. In the first, the jet was turned off and the computation was continued in time. The solution returned toward the symmetric state. In the second experiment, the jet strength was reduced to half its original value and the computation was continued. The resulting flow evolved toward a smaller asymmetry.

Fig. 13 Surface flow pattern: $M_\infty = 0.2$, $\alpha = 40$ deg, $Re_D = 2 \times 10^5$ (jet at $x/D \approx 0.12$).

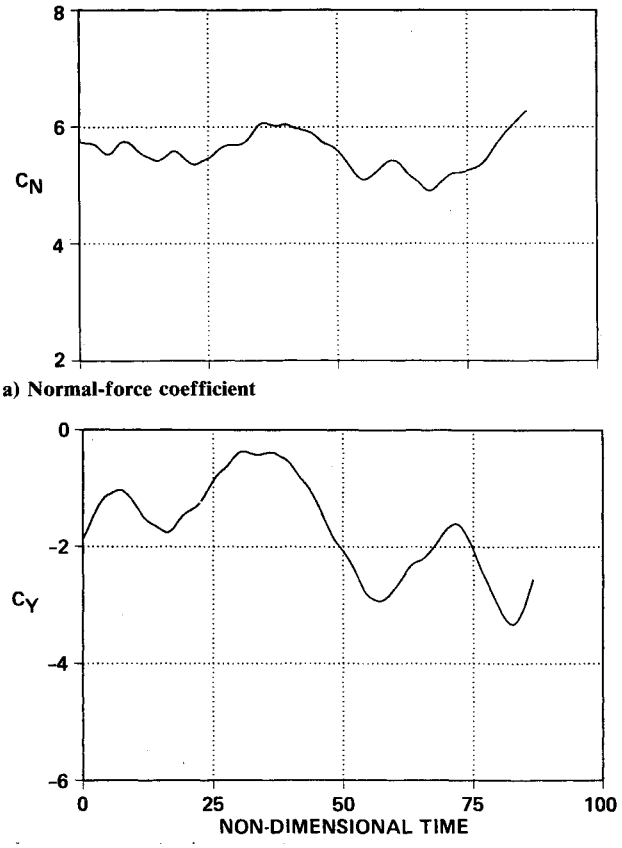

a) Normal-force coefficient

b) Side-force coefficient

Fig. 14 Force coefficient histories: $M_\infty = 0.2$, $\alpha = 40$ deg, $Re_D = 2 \times 10^5$ (jet at $x/D \approx 0.12$).

Case 3 – Asymmetric Flow, Upstream Jet

Several experimental studies of high-incidence flow have suggested that small surface imperfections near the nose can have a large effect on the resulting flow. Recently, Moskovitz et al.[26] showed that various values of side force could be obtained by using various sizes of beads as geometric perturbations. They found that, as the perturbations were located farther from the nose, larger beads were necessary to induce the same degree of flow asymmetry.

To assess the sensitivity of the computed flow to the spatial location of the symmetry-breaking disturbance, in this computation the jet was located closer to the nose ($x/D \approx 0.12$) and had the same strength as in case 2. The effect on the computed flow was much more dramatic. The flowfield became highly asymmetric, as shown in the helicity density contours presented in Fig. 11. The corresponding off-surface streamline pattern (Fig. 12) shows the presence of two pairs of primary vortices. The upstream pair is highly asymmetric and curves away from the body surface near the ogive-cylinder junction in a manner similar to the experimentally observed vortex patterns. Note that the vortex emanating from the near side of the body in Fig. 12 leaves the surface farther downstream. The trailing vortices are not parallel to the freestream, but are inclined approximately 5 deg toward the body from the freestream direction, consistent with the behavior observed experimentally. The computed leeward-side surface flow pattern (Fig. 13) confirms the presence of a large asymmetry where the vortices wash across the leeward meridian to the opposite side of the body.

Time histories of the normal-force and side-force coefficients following a small change in flow conditions are shown in Figs. 14a and 14b, respectively. As was seen in case 1, the flowfield is unsteady and several dominant frequencies can be noted. The oscillations in the normal force are small compared to the mean value of the coefficient. However, the side-force coefficient (Fig. 14b) undergoes a much larger excursion in response to the kick occurring at time zero and appears to evolving toward an oscillation about a mean value of -2.5. The mean side force in this case is approximately half as large as the normal force and is about 350 times larger than the net force due to the jet itself.

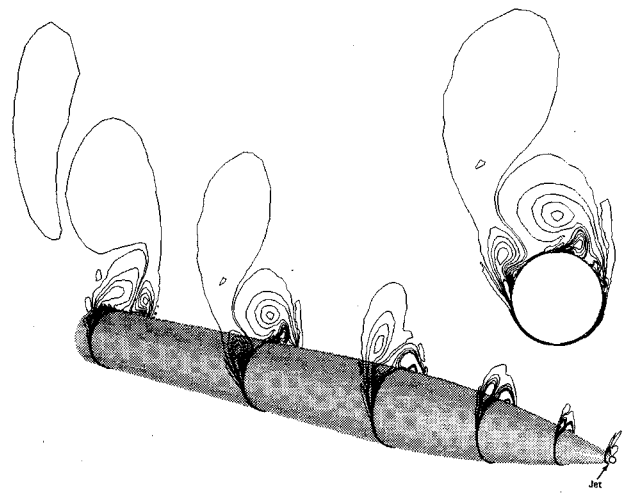

Fig. 15 Helicity density contours: $M_\infty = 0.2$, $\alpha = 40$ deg, $Re_D = 2.6 \times 10^4$ (jet at $x/D \approx 0.12$).

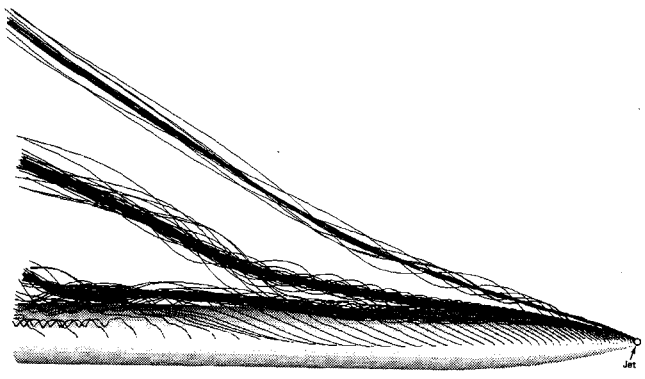

Fig. 16 Off-surface streamlines: $M_\infty = 0.2$, $\alpha = 40$ deg, $Re_D = 2.6 \times 10^4$ (jet at $x/D \approx 0.12$).

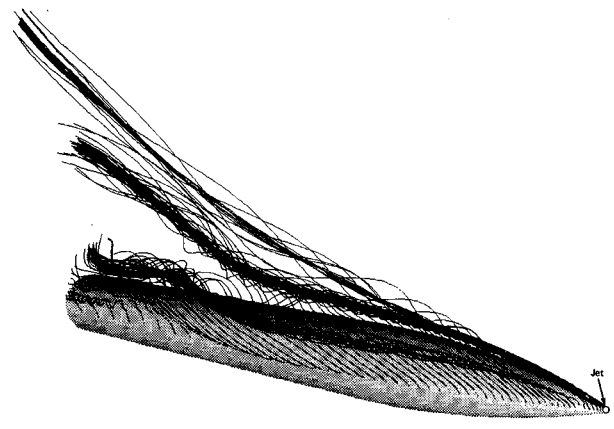

Fig. 17 Off-surface streamlines, front quarter view: $M_\infty = 0.2$, $\alpha = 40$ deg, $Re_D = 2.6 \times 10^4$ (jet at $x/D \approx 0.12$).

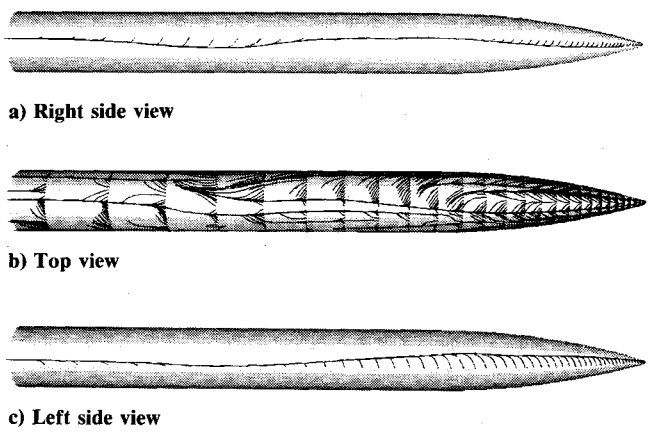

a) Right side view

b) Top view

c) Left side view

Fig. 18 Surface flow pattern: $M_\infty = 0.2$, $\alpha = 40$ deg, $Re_D = 2.6 \times 10^4$ (jet at $x/D \approx 0.12$).

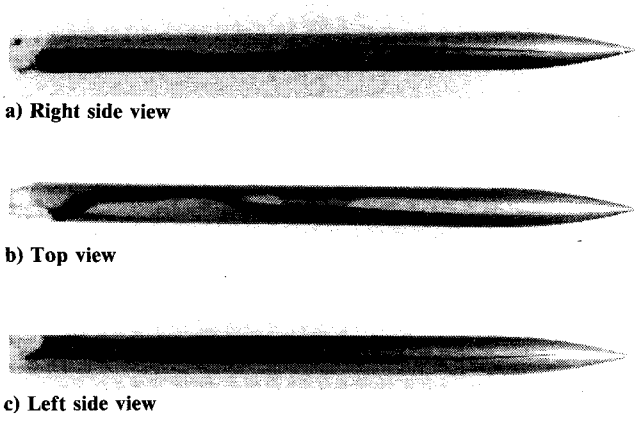

a) Right side view

b) Top view

c) Left side view

Fig. 19 Experimental oil-flow pattern: $\alpha = 40$ deg, $Re_D = 2.6 \times 10^4$ (Ref. 25).

Case 4 – Asymmetric Flow, $Re_D = 2.6 \times 10^4$

In this case, the Reynolds number was changed to $Re_D = 2.6 \times 10^4$ to match the experimental conditions of Degani and Zilliac[22,25] and the jet was located at $x/D \approx 0.12$. In general, the flowfield looks similar to that obtained in case 3 (see Figs. 15–17). However, small differences can be observed in the off-surface streamline pattern shown in Fig. 16. By comparing Fig. 16 with Fig. 12, one can see that the upstream pair of vortices curves away from the body surface farther downstream in the lower Reynolds number case. This is consistent with the behavior observed experimentally by Lamont,[13] who found that as Reynolds number was reduced from 1.25 to 0.20×10^6 the first maximum in the measured side-force distribution moved downstream.

A front quarter view of the off-surface streamlines is shown in Fig. 17. The analogous surface flow pattern is shown in Figs. 18. The asymmetric disposition of the leeward vortices can be clearly seen. The downstream vortex from the far (right) side of the body is seen to lie close to the body surface and to curve across the leeward meridian in an s-shaped curve. The effect this vortex has on the surface flow can be seen in the top view shown in Fig. 18b. The computed patterns are strikingly similar to the experimental surface oil flow visualizations[25] shown in Fig. 19. Although the computed results are not in perfect agreement with the experiments, the main features of the computed flow structure appear to be correct.

The $Re_D = 2.6 \times 10^4$ computation was started from a solution obtained for $Re_D = 2 \times 10^5$. Time histories of the normal-force and side-force coefficients following the change in Reynolds number are shown in Figs. 20a and 20b, respectively. In contrast to case 3 (Figs. 14), the increased laminar viscosity

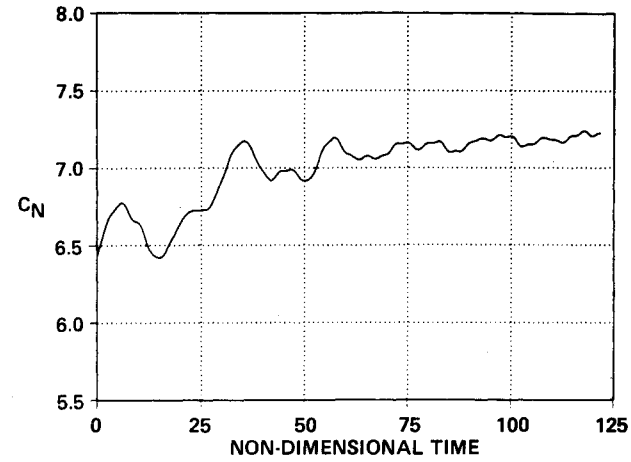

a) Normal-force coefficient

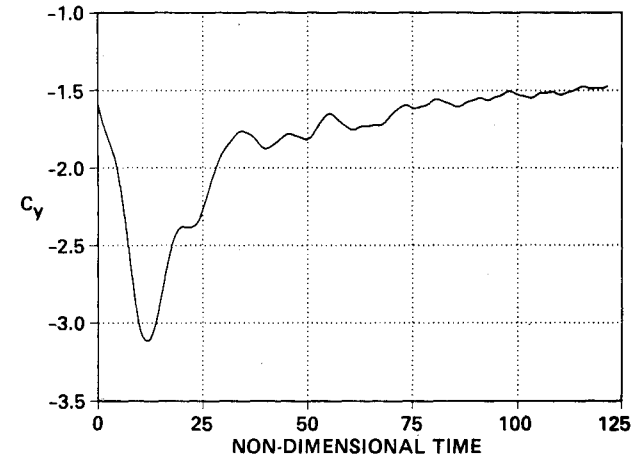

b) Side-force coefficient

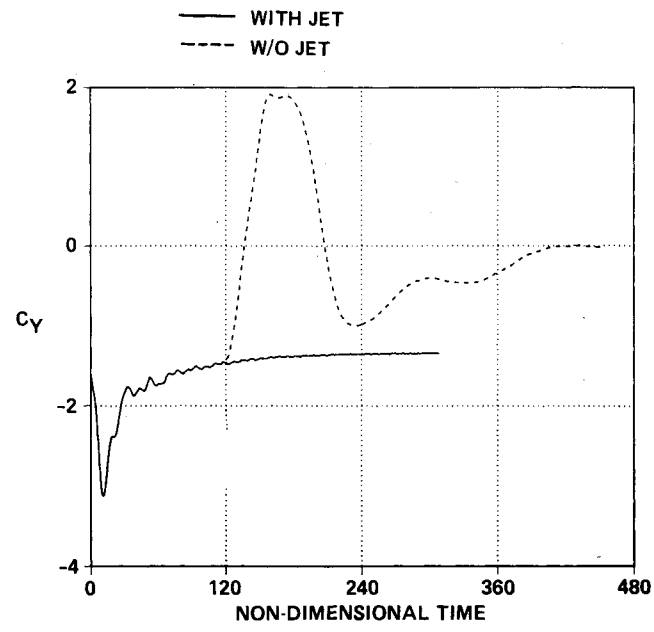

c) Side force coefficients with and without jet.

Fig. 20 Force coefficient histories: $M_\infty = 0.2$, $\alpha = 40$ deg, $Re_D = 2.6 \times 10^4$ (jet at $x/D \approx 0.12$).

causes the normal and side forces tend to decay smoothly and relatively quickly toward constant values, with only small-scale fluctuations. The mean value of the side-force coefficient tends toward -1.5, which is about 200 times larger than the net force due to the jet itself.

In computations of two-dimensional flow about cylinders, it has been found that once unsteady asymmetric vortex shedding is initiated the perturbation can be removed. The vortex shedding will continue without the need for any further perturbations. In order to assess whether the same trend exists for a well-established steady three-dimensional flow (that is, whether the asymmetry would persist in the absence of the perturbation), two cases were run starting at nondimensional time = 120. In one case, the jet was turned off at $t = 120$, and in the other, the jet was continued at the level it had prior to $t = 120$. Time histories of the resulting side-force coefficients are shown in Fig. 20c. The solution with the jet evolved to a side-force coefficient of ≈ -1.4. However, in marked contrast to the behavior observed for two-dimensional cylinder flow, when the jet was turned off, the asymmetric flow returned to a symmetric state.

The fluctuations of the overall forces are moderate in comparison with those observed at the higher Reynolds number, and those fluctuations are not periodic. However, on examining time histories of surface pressure obtained at discrete points along the body, one can see relatively large fluctuation in the pressures. These fluctuations differ, depending on the axial and circumferential location at which they are obtained. Undoubtedly, the fluctuations observed at a point are linked to the mean structure of the asymmetric flow existing above that point.

Discussion and Conclusions

The computational results presented earlier demonstrate, for the first time, the marked asymmetry that has been observed experimentally on slender bodies of revolution at large incidence. The following observations can be drawn from the thin-layer Navier-Stokes results:

1) In the absence of a space-fixed, time-invariant, symmetry-breaking perturbation, the computed solutions for flow around bodies of revolution at large incidence do not become asymmetric, in contrast to the asymmetry observed experimentally.

2) The computed symmetric flows are stable to time-varying perturbations. Even after an asymmetric solution develops in response to a perturbation, removing the perturbation causes the asymmetric flow to relax to the original symmetric state.

3) The effectiveness of a given strength perturbation is a strong function of its point of application. A perturbation applied close to the nose induces a much greater asymmetry than the same perturbation applied farther downstream.

The observation that different degrees of asymmetry can be obtained computationally is also consistent with the experimental data base. Experimental studies of bodies of revolution have shown that multiple values of side force can be obtained at a fixed angle of attack depending on the roll orientation of the body. In particular, Lamont[12,13] and Dexter and Hunt[14] found evidence of near-symmetric flows at angles of attack where most of their measurements showed large asymmetry. Hall,[15] analyzing Lamont's data, showed the existence of a range of side force values at fixed incidence. These findings are consistent with the idea that space-fixed surface roughness elements are inducing the asymmetry. As the body roll angle was varied in the experiments, the surface roughness pattern changed relative to the oncoming flow. Rapid growth, with increasing distance downstream, of the perturbations induced by the roughness elements within the boundary layer, amplify the effect of the roughness to cause the resulting large asymmetry in the vortex pattern. Further, Moskovitz et al.[26] have shown that different degrees of asymmetry can be obtained experimentally by varying the size of a surface disturbance at a fixed location on a slender body. They also have shown that surface disturbances were more effective in inducing asymmetry when placed close to the nose.

The present computational results parallel the experimental findings and explain why asymmetry is almost always observed in the experiments. Despite all possible care taken in constructing a model, small irregularities (large compared to the adjoining boundary-layer thickness) will exist near the tip. Taken together, the computational and experimental observations lead us to believe that three-dimensional vortex asymmetry on slender bodies at large incidence is forced by space-fixed, time-fixed disturbances, such as those due to surface roughness.

Acknowledgments

The authors wish to acknowledge the interest and support of the U.S. Army Ballistic Research Laboratory in conducting this investigation. In addition, we wish to thank Murray Tobak and Gregory Zilliac for their helpful discussions. We would also like to thank Yuval Levy and Ori Degani for their assistance in preparing the graphical representations of the computed flows.

References

[1]Hunt, B. L., "Asymmetric Vortex Wakes on Slender Bodies," AIAA Paper 82-1336, Aug. 1982

[2]Ericsson, L. E., and Reding, J. P., "Aerodynamic Effects of Asymmetric Vortex Shedding from Slender Bodies," AIAA Paper 85-1797, Aug. 1985.

[3]Thomson, K. D., and Morrison, D. F., "The Spacing, Position, and Strength of Vortices in the Wake of Slender Cylindrical Bodies at Large Incidence," *Journal of Fluid Mechanics*, Vol. 50, Pt. 4, 1971, pp. 751–783.

[4]Chapman, G. T., and Tobak, M., "Bifurcations in Unsteady Aerodynamics—Implications for Testing," NASA TM 100083, March 1988.

[5]Patel, V. A., "Karman Vortex Street Behind a Circular Cylinder by the Series Truncation Method," *Journal Computational Physics*, Vol. 28, 1978, pp. 14–42.

[6]Lecointe, Y., and Piquet, J., "On the Use of Several Compact Methods for the Study of Unsteady Incompressible Viscous Flow Round a Circular Cylinder," *Computer & Fluids*, Vol. 12, No. 4, 1984, pp. 25–280.

[7]Rosenfeld, M., Kwak, D., and Vinokur, M., "A Solution Method for the Unsteady and Incompressible Navier-Stokes Equations in Generalized Coordinate Systems," AIAA Paper 88-0718, Jan. 1988.

[8]Degani, D., and Schiff, L. B., "Numerical Simulation of Asymmetric Vortex Flows Occurring on Bodies of Revolution at Large Incidence," AIAA Paper 87-2628, Aug. 1987.

[9]Steger, J. L., Ying, S. X., and Schiff, L. B., "A Partially Flux-Split Algorithm for Numerical Simulation of Unsteady Viscous Flows," *Proceedings of a Workshop on Computational Fluid Dynamics*, Univ. of California, Davis, CA, 1986.

[10]Graham, J. E., and Hankey, W. L., "Computation of the Asymmetric Vortex Pattern for Bodies of Revolution," AIAA Paper 82-0023, Jan. 1982.

[11]Zilliac, G. G., "A Computational/Experimental Study of the Vortical Flow Field on a Body of Revolution at Angle of Attack," AIAA Paper 87-2277, Aug. 1987.

[12]Lamont, P. J., "Pressure Around an Inclined Ogive Cylinder with Laminar, Transitional, or Turbulent Separation," *AIAA Journal*, Vol. 20, No. 11, 1982, pp. 1492–1499.

[13]Lamont, P. J., "The Complex Asymmetric Flow Over a 3.5D Ogive Nose and Cylindrical Afterbody at High Angles of Attack," AIAA Paper 82-0053, Jan. 1982.

[14]Dexter, P. C., and Hunt, B. L., "The Effects of Roll Angle on the Flow over a Slender Body of Revolution at High Angles of Attack," AIAA Paper 81-0358, Jan. 1981.

[15]Hall, R. M., "Forebody and Missile Side Forces and the Time Analogy," AIAA Paper 87-0327, Jan. 1987.

[16]Keener, E. R., Chapman, G. T., Cohen, L., and Taleghani, J., "Side Forces on Forebodies at High Angles of Attack and Mach Numbers From 0.1 to 0.7: Two Tangent Ogives, Paraboloid and Cone," NASA TM X-3438, Feb. 1977.

[17]Viviand, H., "Conservative Forms of Gas Dynamics Equations," *La Recherche Aerospatiale*, No. 1, 1974, pp. 65–68.

[18]Baldwin, B. S., and Lomax, H., "Thin Layer Approximation and Algebraic Model for Separated Turbulent Flows," AIAA Paper 78-257, Jan. 1978.

[19]Steger, J. L., "Implicit Finite-Difference Simulation of Flow About Arbitrary Two-Dimensional Geometries," *AIAA Journal*, Vol. 16, No. 7, 1978, pp. 679–686.

[20]Steger, J. L., and Warming, R. F., "Flux Vector Splitting of the Inviscid Gasdynamic Equations with Applications to Finite-Difference Methods," *Journal of Computational Physics*, Vol. 40, No. 2, 1981, pp. 263–293.

[21]Ying, S. X., "Three-Dimensional Implicit Approximately Factored Schemes for Equations in Gasdynamics," Ph.D. Dissertation, Stanford Univ., Stanford, CA, June 1986.

[22]Degani, D., and Zilliac, G. G., "Experimental Study of Unsteadiness of the Flow Around an Ogive-Cylinder at Incidence," AIAA Paper 88-4330, Aug. 1988.

[23]Schiff, L. B., Degani, D., and Gavali, S., "Numerical Simulation of Vortex Unsteadiness on Slender Bodies of Revolution at Large Incidence," AIAA Paper 89-0195, Jan. 1989.

[24]Levy, Y., Seginer, A., and Degani, D., "Graphical Representation of Three-Dimensional Vortical Flows by Means of Helicity Density and Normalized Helicity," AIAA Paper 88-2598, June 1988.

[25]Degani, D., And Zilliac, G. G., private communication, 1988.

[26]Moskovitz, C. A., Hall, R. M., and DeJarnette, F. R., "Effects of Surface Perturbations on the Asymmetric Vortex Flow Over a Slender Body," AIAA Paper 88-0483, Jan. 1988.

Notice to Authors

When submitting manuscripts to the *AIAA Journal*, please note the new address to which they should be mailed: Dr. George W. Sutton, Kaman Aerospace, 5055 East Broadway Boulevard, Suite C104, Tucson, AZ 85711.